Chinese Physics Letters

Coexisting commensurate pair density waves in 6*R*-TaS_2

To cite this article before publication: Hongqin Xiao *et al* 2026 *Chinese Phys. Lett.* in press https://doi.org/10.1088/0256-307X/43/6/060713

Coexisting commensurate pair density waves in 6*R*-TaS_2

Hongqin Xiao(肖洪钦)[1,2#], Yuxuan He(何昱萱)[1,2#], Ke Zhu(祝轲)[1,2#], Yuhan Ye(耶郁晗)[1,2,3], Yumeng Li(李雨萌)[1,2], Lijing Huang(黄丽静)[1,2], Pucen Xiong(熊浦岑)[1,2], Haitao Yang(杨海涛)[1,2,3], Geng Li(李更)[1,2,3*], and Hong-Jun Gao(高鸿钧)[1,2,3]

[1] *Beijing National Center for Condensed Matter Physics and Institute of Physics, Chinese Academy of Sciences, Beijing 100190, China*

[2] *School of Physical Sciences, University of Chinese Academy of Sciences, Beijing 100190, PR China*

[3] *Hefei National Laboratory, Hefei 230088, China*

Transition metal dichalcogenides (TMDs) hosting multiple intertwined electronic orders provide an important platform for exploring the interplay between competing quantum phases. The non-centrosymmetric 6*R*-TaS_2 features an alternating stacking of 1*T* and 1*H* layers, integrating the electron correlation of the 1*T* phase, superconductivity of the 1*H* phase, and their distinct charge density wave (CDW) states within a single material. However, despite these rich ingredients, the microscopic interplay between CDW order and superconductivity in 6*R*-TaS_2 remains largely unexplored. Here we report scanning tunneling microscopy/spectroscopy measurements on the 1*H* surface of 6*R*-TaS_2, revealing a spatially modulated superconducting gap. Fourier analysis uncovers two coexisting commensurate pair density wave (PDW) orders: an $1a_0 \times 1a_0$ modulation locked to the atomic lattice and a $3a_0 \times 3a_0$ modulation intertwined with the CDW state. The coexistence of these two sets of PDWs indicates a strong coupling between superconductivity and the underlying electronic superstructures. Our results provide direct spectroscopic evidence for intertwined superconducting orders and establish 6*R*-TaS_2 as a unique platform for investigating unconventional pairing states in layered quantum materials

Keywords: Transition metal dichalcogenides, superconductivity, charge density wave, pair density wave

[#]These authors contributed equally to this work.

[*]Correspondence to: gengli.iop@iphy.ac.cn.

Transition metal dichalcogenides (TMDs), particularly the Group V compounds MX_2 (M = Nb, Ta; X = S, Se), provide an important platform for investigating the intricate interplay between charge density waves (CDWs) and superconductivity (SC) in low-dimensional systems.[1-3] Their electronic properties are highly sensitive to structural polymorphs, dimensionality, and electronic correlations. For instance, the 2*H*-polytypes, such as 2*H*-$NbSe_2$ and 2*H*-TaS_2, represent prototypical systems where CDW and SC coexist, raising long-standing questions about whether these orders compete or cooperate.[4-6] In contrast, the 1*T*-polytypes, most notably 1*T*-TaS_2 and 1*T*-$TaSe_2$, host robust commensurate CDW states[7] driven by strong electron-phonon coupling and electronic correlations, which can further give rise to Mott insulating phases and quantum spin-liquid candidates.[8-12]

Beyond these conventional broken-symmetry states, the search for intertwined electronic orders, where multiple order parameters are intimately coupled, has attracted significant interest. Pair density wave (PDW) is one such exotic superconducting state, characterized by a periodic spatial modulation of the superconducting order parameter, which is often found intertwined with charge density wave instabilities. A particularly attractive platform is provided by mixed-polytype compounds with alternating layer stacking. 4*Hb*-TaS_2 integrates the strongly correlated physics of 1*T* layers[13-15] with the superconductivity of 1*H* layers,[16] giving rise to a variety of emergent phenomena including time-reversal symmetry breaking (TRSB)[17] and signatures of topological superconductivity.[18,19] Building on these findings, the non-centrosymmetric 6*R*-TaS_2 provides a distinct intrinsic platform. While it also features alternating 1*T*/1*H* stacking, the absence of inversion symmetry fundamentally differentiates it from the centrosymmetric 4*Hb* phase.[20-25] Such broken inversion symmetry can lead to unconventional superconducting order parameters, including an admixture of spin-singlet and spin-triplet pairing states.[26-28] The mixed-parity states have been proposed to host exotic phenomena such as topological superconductivity and Majorana zero modes.[29-33] Despite these intriguing prospects, the microscopic interplay between CDW order and superconductivity in 6*R*-TaS_2 remains largely unexplored. Recent macroscopic transport measurements have established that 6*R*-TaS_2 undergoes a robust CDW transition at $T_{CDW} \sim 299$ K, followed by a superconducting transition at $T_C \sim 1.94$ K.[22]

In this letter, we report the direct visualization of intertwined electronic orders in the non-centrosymmetric van der Waals superlattice 6*R*-TaS_2 using ultra-low temperature STM/S. Spectroscopic imaging on the 1*H* termination reveals a spatially modulated superconducting gap.

Fourier analysis uncovers two coexisting commensurate pair density wave orders, consisting of an $1a_0 \times 1a_0$ modulation locked to the atomic lattice and a $3a_0 \times 3a_0$ modulation intertwined with the CDW states. These results reveal a strong coupling between superconductivity and the underlying electronic superstructures and establish 6*R*-TaS_2 as a unique platform for exploring intertwined superconducting orders in non-centrosymmetric systems.

The 6*R*-TaS_2 crystallizes in a rhombohedral structure with the R3m space group, characterized by a unique alternating stacking sequence of 1*T* and 1*H* layers along the c-axis.[34] As schematically illustrated in Fig. 1(a), where the blue and orange spheres represent Ta and S atoms respectively, this heterogeneous stacking provides an intriguing platform for investigating the interplay between distinct electronic orders within a single crystal. Upon *in-situ* cleavage at cryogenic temperatures, the crystal tends to break between the weakly bonded S-S layers, allowing two distinct terminating surfaces to be identified by scanning tunneling microscopy (STM).

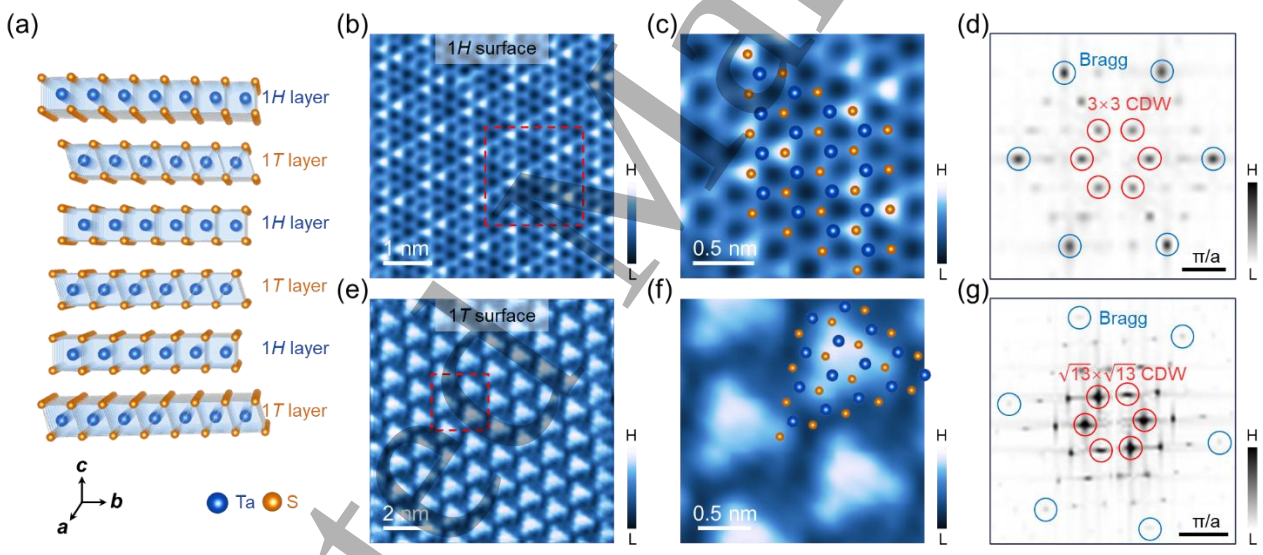

Fig. 1. Crystal structure and STM characterization of the cleaved surfaces of 6*R*-TaS_2. (a) Schematic crystal structure of 6*R*-TaS_2, showing the alternating stacking of 1*T* and 1*H* layers along the c-axis. Blue and orange spheres represent Ta and S atoms, respectively. (b) Atomically resolved STM topographic image of the cleaved 1*H* surface (V_s=-90 mV, I_t=1 nA). (c) Zoomed-in view of the red dashed box in (b) with atomic lattice overlay. (d) Fourier transform (FFT) pattern of (b), marking the atomic Bragg (blue circles) and 3×3 CDW (red circles) peaks. (e) STM topography of the 1*T* surface exhibiting characteristic Star-of-David clusters (V_s =-50 mV, I_t =1 nA). (f) Zoomed-in view of the red dashed box in (e). (g) FT pattern of (e), clearly showing the Bragg (blue circles) and the $\sqrt{13} \times \sqrt{13}$ CDW (red) peaks.

The 1*H* terminating surface exhibits a well-defined hexagonal atomic lattice in the topographic image (Fig. 1(b)). A high-resolution, zoomed-in view in Fig. 1(c) clearly resolves the triangular arrangement of the topmost S atoms. The corresponding Fourier transform (FT) image displays sharp Bragg peaks (indicated by blue circles) associated with the atomic lattice (Fig. 1(d)). Notably, additional 3×3 superlattice peaks (marked by red circles) are observed, which are attributed to the charge density wave instability inherent to the 1*H* surface. The CDW superstructure feature is also clearly resolved in differential conductance pattern (Fig. S1). In contrast, the 1*T* surface displays the characteristic Star-of-David (SoD) clusters (Figs. 1(e) and 1(f)), a hallmark of the strong electron-electron correlation. The FT image of the 1*T* surface (Fig. 1(g)) exhibits a more complex diffraction symmetry, where the $\sqrt{13}\times\sqrt{13}$ CDW peaks (red circles) appear alongside the primary Bragg peaks. These observations confirm the high quality of the 6*R*-TaS_2 single crystals and the layer-dependent electronic structures.

Having characterized the surface morphology and charge orders, we now turn to the local electronic structure of the 1*H* surface using scanning tunneling spectroscopy (STS). To obtain a comprehensive understanding of the local density of states (LDOS) near the Fermi level (E_F), we first performed spectroscopic measurements over a wide energy range. Figure 2(a) displays a typical STM topographic image, with the red arrow indicating the location of the spectroscopic line profile. The spatial evolution of the differential conductance spectra along this path is presented in the waterfall plot in Fig. 2(b) and the corresponding intensity map in Fig. 2(c). As shown in the averaged spectrum (red curve in Fig. 2(d)), the wide-range LDOS exhibits a pronounced V-shaped background with finite conductance at zero bias. This suppression of DOS near E_F is characteristic of the metallic state of 1*H*-TaS_2 under the influence of the CDW gap of approximately 100 meV, consistent with the previously reported spectroscopic feature in 1*H*-TaS_2[19] and 2*H*-TaS_2.[35,36]

To investigate the superconducting gap, we performed high-resolution atomic-scale STS measurements within a narrow energy window (±5 mV). Figure 2(e) displays the topography for this low-energy survey, where the red arrow indicates the spectroscopic line profile. The resulting spatial evolution of the spectra (Fig. 2(f),(g)) unambiguously demonstrates the existence of a robust and uniform energy gap at the Fermi level along the line profile, indicating a coherent superconducting

condensate on the 1*H* surface. In stark contrast, high-resolution STS on the 1*T* surface reveals no superconducting gap but rather a Kondo-like feature (Fig. S2), further confirming that the superconducting condensate is strictly confined to the 1*H* layers. A detailed inspection of the averaged low-energy spectrum in Fig. 2(h) reveals a V-shaped gap feature. Beyond the superconducting gap at ultra-low energy, a shoulder-like feature is resolved near -2 mV (Fig. 2(h) and Fig. S3), which might be related to a hidden magnetic order. Recent transport studies on 6*R*-TaS_2 revealed that this hidden magnetism involves a giant anomalous Hall effect and Kondo screening arising from the coupling between 1*T* and 1*H* layers.[22] This feature likely represents a spectroscopic signature of localized magnetic moments or Kondo hybridization, suggesting a nontrivial interplay between the superconducting condensate and underlying magnetic correlations.

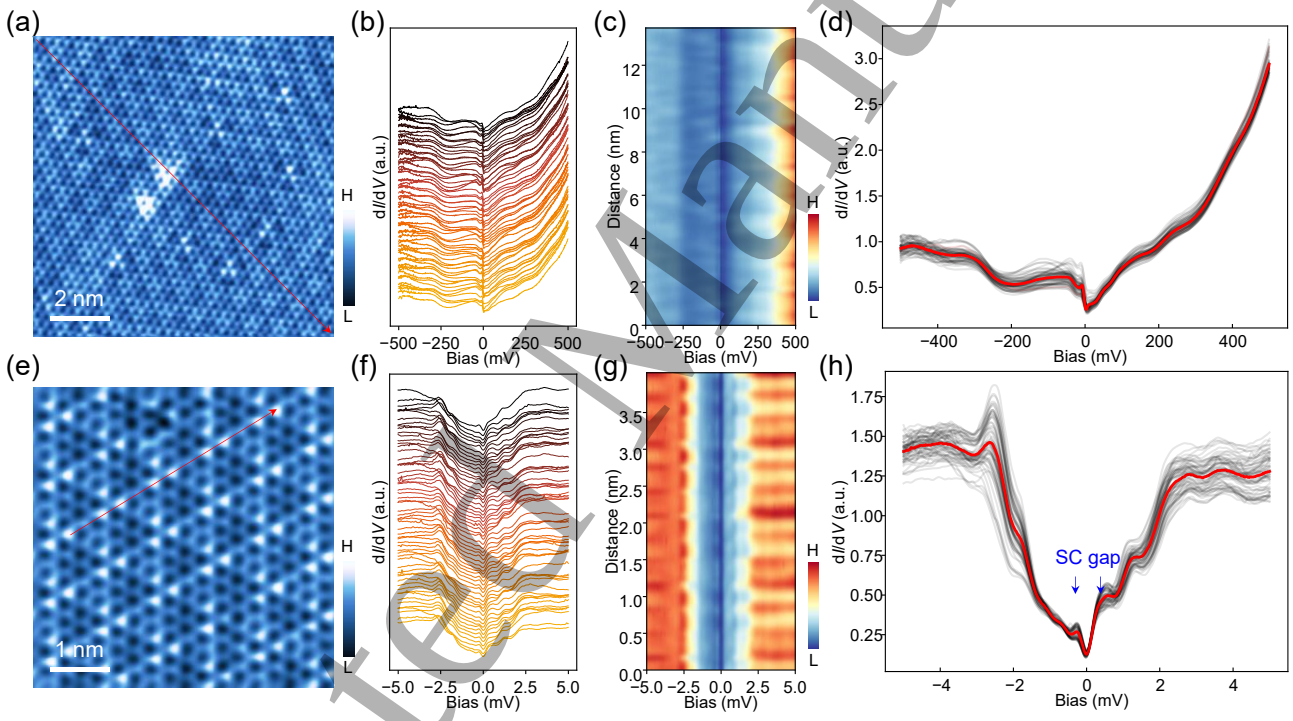

Fig. 2. Spatially resolved differential conductance spectra of the 1*H* surface. (a) Typical STM topography of 1*H* surface. (b),(c) Waterfall plot and intensity map of the wide-range d*I*/d*V* spectra acquired along the red arrow in (a). (d) Averaged wide-range spectrum (red) and the individual spectrum (gray). (e) Another typical STM topography of 1*H* surface. (f),(g), High-resolution waterfall plot and intensity map of the low-energy d*I*/d*V* spectra along the red arrow in (e). (h) Averaged superconducting spectrum (red) and the individual spectrum (gray). The blue arrows mark the superconductivity coherence peaks.

To further elucidate the microscopic nature of the superconducting state and its interplay with the underlying lattice potential, we performed a detailed spatially resolved spectroscopic survey on the 1*H* surface. Fig. 3(a) displays the atomically resolved STM topography, with the red arrow indicating the trajectory of the high-resolution d*I*/d*V* linecut. The spatial evolution of the superconducting gap is visualized in the waterfall plot (Fig. 3(b)) and the corresponding color-coded intensity map (Fig. 3(c) and Fig. S4). The d*I*/d*V* spectra exhibit a V-shaped superconducting gap, which signifies a deviation from conventional BCS behavior.[37] Considering the globally broken inversion symmetry in 6*R*-TaS_2, a mixed-parity pairing state possibly account for the observed nodal-like spectroscopic features. Theoretically, the lack of inversion symmetry permits an admixture of spin-singlet and spin-triplet pairing states[26-28]; the resulting triplet component can naturally give rise to the observed V-shape features. Furthermore, the possible existence of a hidden order suggests the potential for time-reversal symmetry breaking (TRSB) and a chiral order parameter, highlighting the exotic nature of superconductivity in this system.

A closer inspection of the spectra reveals a distinct periodic modulation in the energy positions of the coherence peaks. To quantify this gap modulation, we precisely tracked the energy of the coherence peaks for each spectrum along the trajectory. Figure 3(d) presents a zoomed-in view of the coherence peaks; the red dots marking the peak maxima clearly highlight the oscillatory behavior of the gap. To establish a baseline for the pairing strength, the spatially averaged tunneling spectrum (Fig. 3(e)) was symmetrized and analyzed using a standard Dynes function fitting, which accounts for thermal broadening and finite quasiparticle lifetime effects. The local superconducting gap sizes ($\Delta(r)$), extracted from the individual spectra by identifying peak locations, are plotted as a function of spatial distance in Fig. 3(f). The data exhibits a striking atomic-scale oscillation (blue dots) that is well reproduced by a sinusoidal fitting function (solid line), demonstrating that the superconducting order parameter is not uniform but spatially modulated.

To quantify the precise periodicity of this modulation, we performed a one-dimensional Fourier transform (1D-FT) of the spatial gap profile. The resulting power spectrum exhibits a dominant peak at q_{Bragg}, corresponding to the atomic Bragg wave vector (Fig. 3(g)). This reveals a superconducting gap modulation commensurate with the atomic lattice ($1a_0$ periodicity), a hallmark of a commensurate PDW order. Unlike conventional charge density waves that modulate the local charge density, this state

involves a direct spatial modulation of the superconducting order parameter itself, thereby intrinsically breaking translational symmetry of cooper pair density. The robust persistence of this spatial modulation at elevated temperatures confirms it as an intrinsic thermodynamic phase rather than a disorder-induced inhomogeneity. The presence of such a commensurate PDW on the 1*H* surface of 6*R*-TaS_2 implies a robust coupling between the superconducting condensate and the periodic atomic potential, pointing toward an unconventional mechanism for the coexistence of the intertwined CDW and PDW states.

The microscopic origin of PDW and its relationship with CDW remains a subject of intense debate[38,39]. PDW orders have been reported in diverse systems, including high-T_c cuprates[40], kagome superconductors AV_3Sb_5 (*A = K, Rb, Cs*)[41-45], the heavy Fermion superconductor UTe_2[46], and stoichiometric TMDs such as 2*H*-$NbSe_2$[47,48], where the PDW state is often induced by the underlying CDW order. Furthermore, recent advances have uncovered intrinsic pair density wave, pair density modulation states, as well as their interplay with other quantum phases in iron-based superconductors.[49,50] Sublattice cooper-pair density waves have also been identified in monolayer 1*T'*-$MoTe_2$.[51] These discoveries highlight the universality of this phenomenon in systems with strong density wave instabilities. Compared to cuprates and iron-based superconductors where PDW states are often entangled with complex spin degrees of freedom, or the centrosymmetric 2*H*-$NbSe_2$, the non-centrosymmetric 6*R*-TaS_2 offers a distinct platform. While a similar $3a_0\times3a_0$ PDW might intrinsically exist in bulk 2*H*- or isolated 1*H*-TaS_2(as demonstrated in the structurally analogous 2*H*-$NbSe_2$[48]), its experimental observation remains elusive, likely demanding extreme measurement conditions. In 6*R*-TaS_2, its alternating 1*T*/1*H* stacking and broken inversion symmetry provide a clean environment to explore intertwined electronic orders; because the non-superconducting 1*T* layers physically isolate the adjacent 1*H* planes, the observed PDW is an intrinsic bulk property whose manifestation fundamentally reflects the quasi-2D superconducting nature of the 1*H* layers. Most notably, while a $1a_0\times1a_0$ gap modulation has been reported in iron-based superconductors[50], the observation of such an atomic-lattice-commensurate $1a_0\times1a_0$ PDW is unprecedented in TMDs. The unique coexistence of this $1a_0\times1a_0$ state with the $3a_0\times3a_0$ PDW further distinguishes 6*R*-TaS_2 from conventional systems. Crucially, a closer inspection of Fig. 3(f) reveals a deviation from the simple $1a_0$ modulation. This subtle feature motivates further high-resolution investigations to elucidate the specific interplay

between the gap modulation and the CDW order.

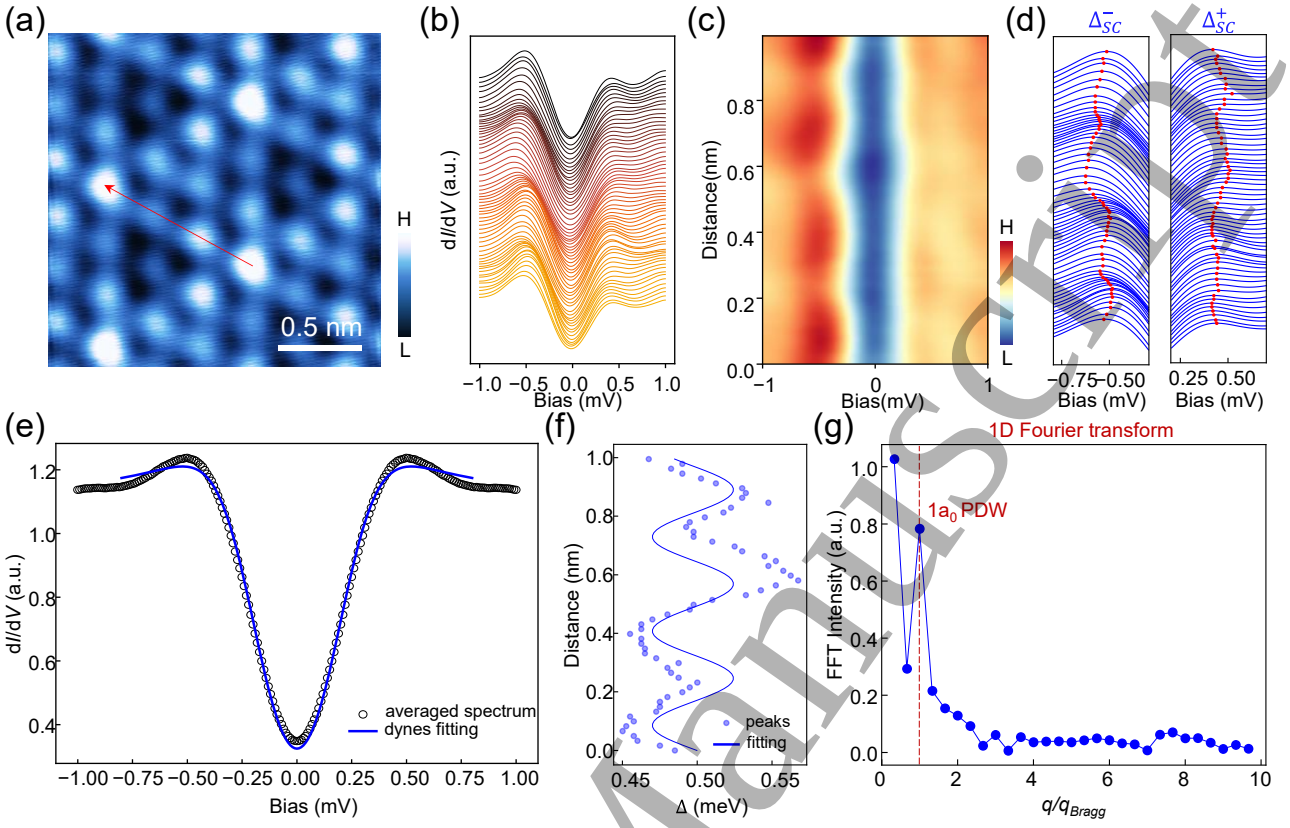

Fig. 3. Observation of $1a_0$ PDW order on the $1H$ surface. (a) Atomically resolved STM topography of $1H$ surface (V_s=-90 mV, I_t=1 nA). (b),(c), Waterfall plot and intensity map of the dI/dV spectra measured along the red arrow, displaying spatial variation of the superconducting gap. (d) Zoomed-in view of the coherence peaks, with red dots tracking the peak positions to highlight the gap modulation. (e) Spatially averaged tunneling spectrum (circles) fitted with a standard Dynes function (blue curve). (f) Spatial evolution of the superconducting gap size Δ (blue dots) and the corresponding sinusoidal fitting (solid line). (g) 1D Fourier transform of the gap modulation profile, exhibiting a peak corresponding to the $1a_0$ PDW order.

Finally, we explore the interplay between the charge density wave and the superconducting condensate by investigating the coexistence of multiple PDW orders on the $1H$ surface. To visualize the spatial correlations between different electronic degrees of freedom, we performed a comparative analysis of the topography, differential conductance, and the local superconducting gap within the same field of view. Figures 4(a)-4(c) display the STM topography, the dI/dV map acquired at 0.5 mV, and the derived superconducting gap map, respectively. In these real-space images, the atomic lattice sites are overlaid

with a structural model, where blue spheres represent Ta atoms and orange spheres represent S atoms. Evidently, the largest superconducting gap occurs at the Ta sites. While the topography and conductance maps are dominated by the atomic lattice and the characteristic 3×3 CDW modulation, the gap map directly reveals the intrinsic spatial texture of the superconducting order parameter.

To quantify the periodicities present in these electronic channels, we performed Fourier transform (FT) analyses of the real-space data. The corresponding reciprocal-space patterns are shown in Figs. 4(d)-4(f). To minimize residual drift originating from temperature fluctuations, the FT images were processed using drift correction followed by six-fold symmetrization. As expected, the FT of the topography (Fig. 4(d)) displays sharp atomic Bragg peaks together with the CDW superlattice vectors. In contrast, the FT of the superconducting gap map (Fig. 4(f)) exhibits a richer structure.

To analyze these periodicities quantitatively, we extracted linecut intensity profiles along the Bragg-peak direction from the six-fold symmetrized FT images (Fig. 4(g)). The resulting profile reveals pronounced peaks at both $q/q_{\mathrm{Bragg}}\approx1/3$ and $q/q_{\mathrm{Bragg}}\approx1$. The peak at $q/q_{\mathrm{Bragg}}\approx1$ indicates a commensurate $a_0\times a_0$ PDW tied to the lattice, while the additional peak at $q/q_{\mathrm{Bragg}}\approx1/3$ provides direct evidence for a $3a_0\times3a_0$ PDW component. The latter is commensurate with the CDW superlattice, suggesting that the superconducting order parameter is modulated simultaneously by the crystal lattice and the electronic superstructure. These observations collectively demonstrate the coexistence of $1a_0\times1a_0$ and $3a_0\times3a_0$ PDW orders, providing compelling evidence for the intertwined nature of charge order and superconductivity in 6*R*-TaS_2.

The discovery of spatially modulated superconducting states in 6*R*-TaS_2 offers an important perspective on the coexistence of charge density waves and pair density waves superconductivity. In particular, the presence of the $3a_0$ modulation demonstrates that the superconducting order parameter is spatially locked to the CDW wave vector, consistent with theoretical proposals in which CDW order can induce PDW components.[52,53] To further elucidate the nature of this intertwining, we consider the distinct phase signatures identified in other systems. For example, in the kagome superconductor CsV_3Sb_5, a $4a_0/3$ roton PDW is proposed as a primary state responsible for the pseudogap , where the coherence peak height $P(r)$ and zero-bias conductance $G_0(r)$ exhibit a characteristic out-of-phase spatial modulation.[41] In contrast, in 2*H*-$NbSe_2$, the PDW is deeply entangled with the CDW configurations; phase analysis reveals that the superconducting gap size $\Delta(r)$ oscillates in-phase with

the charge density while the coherence peak height $H(r)$ presents a significant $2\pi/3$ phase shift.[48] Our 6*R*-TaS_2 system distinguishes itself by the simultaneous coexistence of atomic-lattice-locked ($1a_0\times1a_0$) and CDW-commensurate ($3a_0\times3a_0$) PDW orders, suggesting an exceptionally complex interplay that warrants further phase-sensitive investigation. By visualizing the intricate coupling between these orders, our results establish 6*R*-TaS_2 as a promising system for investigating PDW physics. Furthermore, it highlights the potential of structural polymorphism in tuning electronic correlations, laying a foundation for exploring unconventional superconductivity in non-centrosymmetric quantum materials.

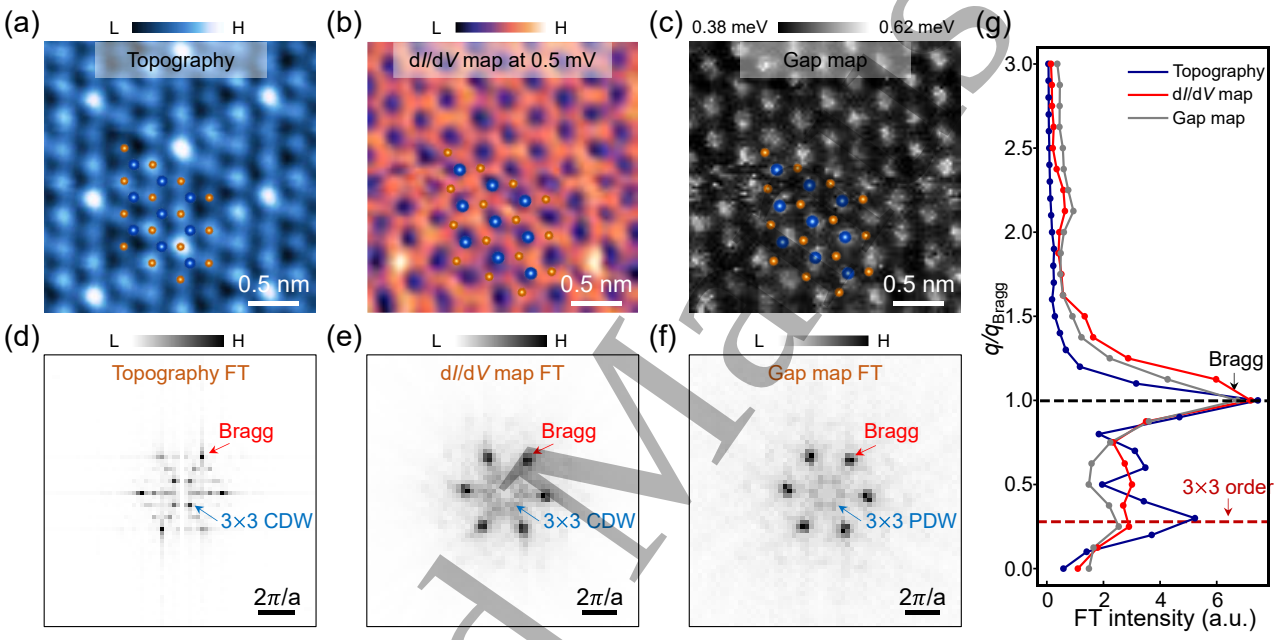

Fig. 4. Coexistence of $1a_0\times1a_0$ and $3a_0\times3a_0$ PDW orders. (a)-(c), Topography (V_s=-90 mV, I_t=1 nA), dI/dV map at 0.5 mV, and superconducting gap map acquired in the same field of view. The superimposed blue and orange dots mark the atomic lattice sites. (d)-(f), Corresponding Fourier transform (FT) patterns of the topography, dI/dV map, and gap map, respectively. The figures are initially drift-corrected and then symmetrized with six-fold symmetry. Locations of CDW(Bragg) points are indicated by blue(red) arrows, respectively. (g), Line-cut intensity profiles extracted from the 6-fold symmetrized FT images along the Bragg point direction. The observation of distinct peaks at both $q/q_{\mathrm{Bragg}} = 1$ and $q/q_{\mathrm{Bragg}} = 1/3$ provides evidence for the coexistence of $1a_0\times1a_0$ and $3a_0\times3a_0$ PDW.

In summary, we have utilized ultra-low temperature STM/S to visualize the electronic states of the van der Waals superlattice 6*R*-TaS_2. Moving beyond structural characterization, our central finding is the

direct observation of a PDW state that is intimately intertwined with the CDW order. We demonstrated that the superconducting gap is not uniform but exhibits a robust spatial modulation that is locked simultaneously to both the atomic lattice ($1a_0 \times 1a_0$) and the electronic superlattice ($3a_0 \times 3a_0$). These results not only deepen our understanding of the cooperative interplay between CDW and superconductivity in TMDs but also highlight the potential of 6*R*-TaS_2 for realizing exotic quantum states.

References

[1] Wilson J A, Di Salvo F J and Mahajan S 1974 *Phys. Rev. Lett.* **32** 882.

[2] Xi X, Zhao L, Wang Z, Berger H, Forró L, Shan J and Mak K F 2015 *Nat. Nanotechnol.* **10** 765.

[3] Sipos B, Kusmartseva A F, Akrap A, Berger H, Forró L and Tutiš E 2008 *Nat. Mater.* **7** 960.

[4] Castro Neto A H 2001 *Phys. Rev. Lett.* **86** 4382.

[5] Sooryakumar R and Klein M V 1980 *Phys. Rev. Lett.* **45** 660.

[6] Zheng F and Feng J 2019 *Phys. Rev. B* **99** 161119.

[7] Cao Z-Y, Chen H, Qian G-J, Shi Y-H, Qi Q, Han X-H, Yang H-T and Gao H-J 2025 *Chin. Phys. Lett.* **42** 100702.

[8] Law K T and Lee P A 2017 *Proc. Natl. Acad. Sci.USA* **114** 6996.

[9] Chen Y, Ruan W, Wu M, Tang S, Ryu H, Tsai H-Z, Lee R L, Kahn S, Liou F, Jia C, Albertini O R, Xiong H, Jia T, Liu Z, Sobota J A, Liu A Y, Moore J E, Shen Z-X, Louie S G, Mo S-K and Crommie M F 2020 *Nat. Phys.* **16** 218.

[10] Cho D, Cheon S, Kim K-S, Lee S-H, Cho Y-H, Cheong S-W and Yeom H W 2016 *Nat. Commun.* **7** 10453.

[11] Huang X, Lado J L, Sainio J, Liljeroth P and Ganguli S C 2025 *Phys. Rev. Lett.* **134** 046504.

[12] Li Y, Xiao Y, Zheng Q, Lin X, Huang L and Gao H-J 2023 *Chin. Phys. B* **32** 077101.

[13] Kumar Nayak A, Steinbok A, Roet Y, Koo J, Feldman I, Almoalem A, Kanigel A, Yan B, Rosch A, Avraham N and Beidenkopf H 2023 *Proc. Natl. Acad. Sci.USA* **120** e2304274120.

[14] Crippa L, Bae H, Wunderlich P, Mazin I I, Yan B, Sangiovanni G, Wehling T and Valentí R 2024 *Nat. Commun.* **15** 1357.

[15] Geng Y Y, Guo J F, Meng F Y, Wang M Y, Mi S, Huang L, Xu R, Pang F, Liu K, Wang S C, Gao H J, Zhou W C, Ji W, Lei H C and Cheng Z H 2024 *Phys. Rev. B* **110** 115107.

[16] Silber I, Mathimalar S, Mangel I, Nayak A K, Green O, Avraham N, Beidenkopf H, Feldman I, Kanigel A, Klein A, Goldstein M, Banerjee A, Sela E and Dagan Y 2024 *Nat. Commun.* **15** 824.

[17] Ribak A, Skiff R M, Mograbi M, Rout P K, Fischer M H, Ruhman J, Chashka K, Dagan Y and Kanigel A 2020 *Sci. Adv.* **6** eaax9480.

[18] Nayak A K, Steinbok A, Roet Y, Koo J, Margalit G, Feldman I, Almoalem A, Kanigel A, Fiete G A, Yan B, Oreg Y, Avraham N and Beidenkopf H 2021 *Nat. Phys.* **17** 1413.

[19] Vaňo V, Amini M, Ganguli S C, Chen G, Lado J L, Kezilebieke S and Liljeroth P 2021 *Nature* **599** 582.

[20] Achari A, Bekaert J, Sreepal V, Orekhov A, Kumaravadivel P, Kim M, Gauquelin N, Balakrishna Pillai P, Verbeeck J, Peeters F M, Geim A K, Milošević M V and Nair R R 2022 *Nano Lett.* **22** 6268.

[21] Lv X, Song H, Chen K, Liu S, Huang Y, Fang Y and Cui T 2023 *arXiv preprint arXiv: 2311.07153*.

[22] Liu S-B, Tian C, Fang Y, Rong H, Cao L, Wei X, Cui H, Chen M, Chen D, Song Y, Cui J, Li J, Guan S, Jia S, Chen C, He W, Huang F, Jiang Y, Mao J, Xie X C, Law K T and Chen J-H 2024 *Nat. Commun.* **15** 7569.

[23] Pal S, Bahera P, Sahu S R, Srivastava H, Srivastava A K, Lalla N P, Sankar R, Banerjee A and Roy S B 2023 *Physica. B* **669** 415266.

[24] Yan L M, Bu K J, Li Z Y, Zhang Z H, Xia W, Li M T, Li N N, Guan J Y, Liu X Q, Ning J H, Zhang D Z, Guo Y F, Wang X and Yang W E 2024 *Nano Lett.* **24** 6002.

[25] Wang S P, Han Y Y, Sun S T, Wang S Y, An C, Chen C H, Zhang L L, Zhou Y H, Zhou J and Yang Z R 2024 *Phys. Rev. Lett.* **133** 056001.

[26] Smidman M, Salamon M B, Yuan H Q and Agterberg D F 2017 *Rep. Prog. Phys.* **80** 036501.

[27] Zhou B T, Yuan N F Q, Jiang H-L and Law K T 2016 *Phys. Rev. B* **93** 180501.

[28] Wan Z, Qiu G, Ren H, Qian Q, Li Y, Xu D, Zhou J, Zhou J, Zhou B, Wang L, Yang T-H, Sofer Z, Huang Y, Wang K L and Duan X 2024 *Nature* **632** 69.

[29] Li M, Li G, Cao L, Zhou X, Wang X, Jin C, Chiu C-K, Pennycook S J, Wang Z and Gao H-J 2022 *Nature* **606** 890.

[30] Wang D, Kong L, Fan P, Chen H, Zhu S, Liu W, Cao L, Sun Y, Du S, Schneeloch J, Zhong R, Gu G, Fu L, Ding H and Gao H-J 2018 *Science* **362** 333.

[31] Zhu S, Kong L, Cao L, Chen H, Papaj M, Du S, Xing Y, Liu W, Wang D, Shen C, Yang F, Schneeloch J, Zhong R, Gu G, Fu L, Zhang Y-Y, Ding H and Gao H-J 2020 *Science* **367** 189.

[32] Kong L, Zhu S, Papaj M, Chen H, Cao L, Isobe H, Xing Y, Liu W, Wang D, Fan P, Sun Y, Du S, Schneeloch J, Zhong R, Gu G, Fu L, Gao H-J and Ding H 2019 *Nat. Phys.* **15** 1181.

[33] Cao L, Li G, Liu W, Liu Y-B, Chen H, Xing Y, Kong L, Yang F, Hu Q, Li M, Zhou X, Chen Z, Ke C, Hu L, Cao G-H, Wu C, Ding H and Gao H-J 2024 *Chin. Phys. Lett.* **41** 117401.

[34] Thompson A H 1975 *Solid State Commun.* **17** 1115.

[35] Hall J, Ehlen N, Berges J, van Loon E, van Efferen C, Murray C, Rösner M, Li J, Senkovskiy B V, Hell M, Rolf M, Heider T, Asensio M C, Avila J, Plucinski L, Wehling T, Grüneis A and Michely T 2019 *ACS Nano* **13** 10210.

[36] Wang C, Giambattista B, Slough C G, Coleman R V and Subramanian M A 1990 *Phys. Rev. B* **42** 8890.

[37] Song C-L, Wang Y-L, Cheng P, Jiang Y-P, Li W, Zhang T, Li Z, He K, Wang L, Jia J-F, Hung H-H, Wu C, Ma X, Chen X and Xue Q-K 2011 *Science* **332** 1410.

[38] Shi X, Liu X, Li G, Zhao Z, Yang H, Lin X and Gao H-J 2025 *Chin. Phys. B* **34** 077101.

[39] Han X, Cao Z, Huang Z, Zhao Z, Yang H, Chen H and Gao H-J 2025 *Chin. Phys. B* **34** 016801.

[40] Edkins S D, Kostin A, Fujita K, Mackenzie A P, Eisaki H, Uchida S, Sachdev S, Lawler M J, Kim E-A, Séamus Davis J C and Hamidian M H 2019 *Science* **364** 976.

[41] Chen H, Yang H, Hu B, Zhao Z, Yuan J, Xing Y, Qian G, Huang Z, Li G, Ye Y, Ma S, Ni S, Zhang H, Yin Q, Gong C, Tu Z, Lei H, Tan H, Zhou S, Shen C, Dong X, Yan B, Wang Z and Gao H-J 2021 *Nature* **599** 222.

[42] Deng H, Qin H, Liu G, Yang T, Fu R, Zhang Z, Wu X, Wang Z, Shi Y, Liu J, Liu H, Yan X-Y, Song W, Xu X, Zhao Y, Yi M, Xu G, Hohmann H, Holbæk S C, Dürrnagel M, Zhou S, Chang G, Yao Y, Wang Q, Guguchia Z, Neupert T, Thomale R, Fischer M H and Yin J-X 2024 *Nature* **632** 775.

[43] Deng H, Liu G, Guguchia Z, Yang T, Liu J, Wang Z, Xie Y, Shao S, Ma H, Liège W, Bourdarot F, Yan X-Y, Qin H, Mielke C, Khasanov R, Luetkens H, Wu X, Chang G, Liu J, Christensen M H, Kreisel A, Andersen B M, Huang W, Zhao Y, Bourges P, Yao Y, Dai P and Yin J-X 2024 *Nat. Mater.* **23** 1639.

[44] Han X, Chen H, Tan H, Cao Z, Huang Z, Ye Y, Zhao Z, Shen C, Yang H, Yan B, Wang Z and Gao H-J 2025 *Nat. Nanotechnol.* **20** 1017.

[45] Chen H, Hu B, Ye Y, Yang H and Gao H-J 2022 *Chin. Phys. B* **31** 097405.

[46] Gu Q, Carroll J P, Wang S, Ran S, Broyles C, Siddiquee H, Butch N P, Saha S R, Paglione J, Davis J C S and Liu X 2023 *Nature* **618** 921.

[47] Liu X, Chong Y X, Sharma R and Davis J C S 2021 *Science* **372** 1447.

[48] Cao L, Xue Y, Wang Y, Zhang F-C, Kang J, Gao H-J, Mao J and Jiang Y 2024 *Nat. Commun.* **15** 7234.

[49] Liu Y, Wei T, He G, Zhang Y, Wang Z and Wang J 2023 *Nature* **618** 934.

[50] Kong L, Papaj M, Kim H, Zhang Y, Baum E, Li H, Watanabe K, Taniguchi T, Gu G, Lee P A and Nadj-Perge S 2025 *Nature* **640** 55.

[51] Cheng F-J, Lou C-C, Chen A-X, Wei L-X, Liu Y, Deng B-Y, Li F, Wang Z, Xue Q-K, Ma X-C and Song C-L 2025 *Phys. Rev. Lett.* **135** 166201.

[52] Agterberg D F, Davis J C S, Edkins S D, Fradkin E, Van Harlingen D J, Kivelson S A, Lee P A, Radzihovsky L, Tranquada J M and Wang Y 2020 *Annu. Rev. Condens. Matter Phys.* **11** 231.

[53] Zhou S and Wang Z 2022 *Nat. Commun.* **13** 7288.

Experimental details

Single-crystal growth

High-quality 6*R*-TaS_2 single crystals were synthesized by using Chemical Vapor Transport techniques, with NH_4Cl as the transport agent. A 6*R*-TaS_2 crystal was mounted on an STM sample holder in a glove box and transferred to an ultra-high vacuum chamber. The crystal was cleaved in-situ at room temperature, and then immediately transferred to an STM scanner.

STM/S experiments

The STM/S measurements were conducted in an ultra low temperature STM system equipped with 9-2-2 T vectorial magnets. Tungsten tips were etched chemically and calibrated on Au(111) surfaces before use. The d*I*/d*V* spectra and maps were obtained by a standard lock-in technique with modulation voltage of 5 mV in Fig. 2(b) and 50 μV in Figs. 2(f), 3 and 4 at 973.1 Hz. All the images and d*I*/d*V* maps were taken at 30 mK.

Acknowledgments

Project supported by the National Key Research and Development Projects of China (2024YFA1207700, 2022YFA1204100), National Natural Science Foundation of China (62488201), the CAS Project for Young Scientists in Basic Research (YSBR-003), the Youth Innovation Promotion Association (2023005), and the Quantum Science and Technology-National Science and Technology Major Project (2021ZD0302700).